Cite as: P. C. Bunting *et al.*, *Science* 10.1126/science.aat7319 (2018).

A linear cobalt(II) complex with maximal orbital angular momentum from a non-Aufbau ground state

Philip C. Bunting[1], Mihail Atanasov[2,3], Emil Damgaard-Møller[4], Mauro Perfetti[5], Iris Crassee[6], Milan Orlita[6,7], Jacob Overgaard[4], Joris van Slageren[5], Frank Neese[2], Jeffrey R. Long[1,8,9]*

[1]Department of Chemistry, University of California, Berkeley, CA 94720, USA. [2]Max-Planck-Insitut für Kohlenforschung, Mülheim an der Ruhr D-45470, Germany. [3]Institute of General and Inorganic Chemistry, Bulgarian Academy of Sciences, Academy Georgi Bontchev, Sofia 1113, Bulgaria. [4]Department of Chemistry and Centre for Materials Crystallography, Aarhus University, DK-8000 Aarhus C, Denmark. [5]Institut für Physikalische Chemie and Center for Integrated Quantum Science and Technology (IQST), Universität Stuttgart, Pfaffenwaldring 55, 70569 Stuttgart, Germany. [6]Laboratoire National des Champs Magnétiques Intenses, CNRS-UGA-UPS-INSA-EMFL, 25 rue des Martyrs, 38042 Grenoble, France. [7]Institute of Physics, Charles University, Ke Karlovu 5, 12116 Praha 2, Czech Republic. [8]Department of Chemical and Biomolecular Engineering, University of California, Berkeley, CA 94720, USA. [9]Materials Sciences Division, Lawrence Berkeley National Laboratory, Berkeley, CA 94720, USA.

***Corresponding author. Email: jrlong@berkeley.edu**

Orbital angular momentum is a prerequisite for magnetic anisotropy, although in transition metal complexes it is typically quenched by the ligand field. Here, by reducing the basicity of the carbon donor atoms in a pair of alkyl ligands, we synthesize a cobalt(II) dialkyl complex, $Co(C(SiMe_2ONaphthyl)_3)_2$, wherein the ligand field is sufficiently weak that interelectron repulsion and spin-orbit coupling play a dominant role in determining the electronic ground state. Assignment of a non-Aufbau $(d_{x^2-y^2}, d_{xy})^3(d_{xz}, d_{yz})^3(d_{z^2})^1$ electron configuration is supported by dc magnetic susceptibility data, experimental charge density maps, and ab initio calculations. Variable-field far-infrared spectroscopy and ac magnetic susceptibility measurements further reveal slow magnetic relaxation via a 450 cm^{-1} magnetic excited state.

All materials exhibiting a large magnetic anisotropy possess nonzero orbital angular momentum L arising from an electronic structure of partially-filled (but not half-filled) energetically degenerate orbitals. In trivalent lanthanide ions, the valence 4f orbitals are well-shielded and interact little with their coordination environment, allowing for a nonzero L that couples with the total spin S to give rise to a total angular momentum of $|L - S| \leq J \leq |L + S|$ and potentially a large magnetic anisotropy. In the case of transition metals, however, the ligand field typically removes any orbital degeneracy, leading to quenching of the orbital angular momentum ($L = 0$) and an appropriate description of the ground state in terms of S only. When magnetic anisotropy is present in such complexes, it is generally a weak effect that arises from mixing of electronic ground and excited states induced by spin-orbit coupling. Creating unquenched orbital angular momentum in molecular transition metal-based systems requires an exceptionally weak ligand field and/or two or more orbitals that are nearly degenerate. In this context, perhaps the simplest experimental system is a one-coordinate cobalt atom: individual cobalt atoms on a MgO surface (referred to as adatoms) were recently shown using scanning probe microscopy to possess a $J = {}^9/_2$ ($L = 3$, $S = {}^3/_2$) ground state and exhibit near maximal magnetic anisotropy in a half-integer spin 3*d* system (*1*).

In the regime of molecules, linearly coordinated transition metal complexes have garnered interest of late because they are energetically unaffected by Jahn-Teller distortions, allowing for the possibility of virtually unquenched orbital angular momentum (*2*). Analogously to lanthanide complexes, such transition metal systems with nonzero L are best described by a total angular momentum J, which is split by spin-orbit coupling and the ligand field into $2J + 1$ M_J states. Two transition metal complexes that have been described using this formalism are the iron(II) complex $Fe(C(SiMe_3)_3)_2$ and the iron(I) complex $[Fe(C(SiMe_3)_3)_2]^-$ (*3*, *4*). Both complexes have ground states with $L = 2$ due to electronic configurations which place three electrons in the degenerate orbital pair $d_{x^2-y^2}$ and d_{xy}, which arise from linear combinations of the hydrogen-like d-orbitals with $m_l = \pm 2$. A notable consequence of these electronic structures is that both complexes exhibit relatively large energy separations between their ground and first excited M_J states, making them prone to single-molecule magnet behavior (*5*). Indeed, ac magnetic susceptibility data revealed that both molecules exhibit slow magnetic relaxation (the former complex under an applied dc field and the latter in zero applied field) with effective spin-reversal barriers (U_{eff}) of 178 and 246 cm^{-1}, respectively (*6*)—values close to the calculated energy separations between their ground and first excited M_J states (*7*, *8*).

At first glance it may seem impossible to increase orbital angular momentum for a transition metal complex beyond L

= 2. An L = 3 ground state requires two sets of degenerate orbitals, $d_{x^2-y^2}$, d_{xy} (m_l = ±2) and d_{xz}, d_{yz} (m_l = ±1), with an odd number of electrons in each. The Aufbau principle describes the manner in which electrons fill orbitals, typically from lowest to highest energy. A more rigorous consideration of electronic structure accounts for three main effects: ligand field stabilization, interelectron repulsion, and spin-orbit coupling. Ligand field effects typically dominate when considering transition metal complexes. When the ligand field stabilization and interelectron repulsion energies are similar in transition metal complexes, high spin electronic configurations arise. For example, placing three electrons in the orbitals ($d_{x^2-y^2}$, d_{xy})(d_{xz}, d_{yz}) could give the low-spin configuration ($d_{x^2-y^2}$, d_{xy})^3(d_{xz}, d_{yz})^0 if the energy separation between orbital pairs is larger than the electron pairing energy, or the high-spin configuration ($d_{x^2-y^2}$, d_{xy})^2(d_{xz}, d_{yz})^1 if the orbital pairs are relatively close in energy. For six electrons, the expected Aufbau filling of these orbitals is ($d_{x^2-y^2}$, d_{xy})^4(d_{xz}, d_{yz})^2, and as the sixth electron must be paired in either orbital pair, there is no reason to assume there would be any stabilization from the non-Aufbau configuration, ($d_{x^2-y^2}$, d_{xy})^3(d_{xz}, d_{yz})^3.

Intriguingly, calculations on the hypothetical complex $Co(C(SiMe_3)_3)_2$ show a ground state with L = 3, which arises from a non-Aufbau 3d-orbital filling of ($d_{x^2-y^2}$, d_{xy})^3(d_{xz}, d_{yz})^3(d_{z^2})^1, and further predict a splitting between ground and first excited M_J states of 454 cm^{-1} (*9*). Efforts to synthesize this molecule both by our laboratory and others (*10*) were unsuccessful. Moreover, although nearly 70 two-coordinate, paramagnetic transition metal complexes have been synthesized (*11*), the only such compounds with alkyl ligands are of the type $[M(C(SiMe_3)_3)_2]^{0/1-}$, where M is Fe(II) (*12*), Fe(I) (4), Mn(II) (*13*) and Mn(I) (*14*). Several approximately linear cobalt(II) complexes have been studied, however, and one such molecule (sIPr)CoNDmp (where sIPr is an N-heterocyclic carbene and NDmp is an arylimido ligand) has a spin-reversal barrier of 413 cm^{-1}, more than 1.5 times that measured for $[Fe^I(C(SiMe_3)_3)_2]^-$, despite both molecules possessing the same total angular momentum of J = $^7/_2$ (*15*). Correspondingly, the increase in magnetic anisotropy for the Co(II) complex must arise from an increase in the spin-orbit coupling constant, a value which trends with effective nuclear charge. In another example, bent $[OCoO]^-$ anions inserted into the channels of an apatite-type structure were shown to have a spin-reversal barrier of 387 cm^{-1} (*16*). A semi-empirical method based on ligand field parameterization predicted that such a barrier could arise from a J = $^9/_2$ ground state, with increasing mixing of M_J states (and a concomitant diminishing of the barrier height) arising as the $[OCoO]^-$ anion becomes increasingly bent. In the extreme case of the cobalt adatoms mentioned above, a separation of 468 cm^{-1} was determined for the separation between M_J = $^9/_2$ and $^7/_2$ states (1).

Our motivations to isolate a dialkyl cobalt(II) complex were thus twofold: first, the proposed electronic structure violates the Aufbau principle and is analogous to what is commonly seen for lanthanides; second, realizing maximal orbital angular momentum should afford a very large magnetic anisotropy, a property that has important applications in the study of magnetism. Here, we present the synthesis and characterization of such a dialkyl cobalt(II) complex and confirm the proposed J = $^9/_2$ ground state through direct electronic and spectroscopic measurements, ab initio modeling, and magnetic susceptibility measurements. The energy separation between the M_J = ±$^9/_2$ and ±$^7/_2$ states leads to slow magnetic relaxation at temperatures as high as 70 K and low-temperature magnetic hysteresis.

Synthesis and structure of a linear cobalt dialkyl complex

Our attempts to synthesize $Co(C(SiMe_3)_3)_2$ from metathesis reactions of $[C(SiMe_3)_3]^-$ salts and CoX_2 (X = Cl, Br, I) gave only intractable amorphous black solids. Similar reactivity with $[C(SiMe_3)_3]^-$ was reported previously, but by switching to $[C(SiMe_2Ph)_3]^-$ it proved possible to isolate the dimer $[Co(C(SiMe_2Ph)_3)]_2$, a product formed by the in situ reduction of cobalt(II) (*10*). Thus, at least one challenge in isolating a dialkyl cobalt(II) complex is the strongly reducing nature of the carbanion. Others have shown that substituting electron-withdrawing alkoxides onto each silyl group significantly reduces the basicity and electron density of the carbanion (*17*). In an initial pursuit of this approach, we found that $[C(SiMe_2OPh)_3]^-$ did support a dialkyl cobalt(II) complex, $Co(C(SiMe_2OPh)_3)_2$, but long-range Co···O interactions led to a significantly bent C–Co–C axis (fig. S1). We next synthesized a number of $[C(SiMe_2OR)_3]^-$ derivatives (R = various alkyl or substituted phenyl groups) following the general reaction scheme outlined in Fig. 1A. Smaller substituents did not readily yield isolable products, and larger substituents supported only dinuclear complexes of the type $(R_3CCo)_2(\mu\text{-}X)_2$ (where X is a halide), similar to the structure of $((PhMe_2Si)_3CZn)_2(\mu\text{-}Cl)_2$ (*18*). In an effort to reduce the nucleophilicity of the oxygen atom, we also tried using electron withdrawing substituents such as perfluorophenyl, but found these ligands to be susceptible to Si–O cleavage, a challenge also encountered when trying to metallate other $HC(SiMe_2OR)_3$ complexes with MeLi (*19*). Ultimately, we determined that only the naphthol (R = Naph = $C_{10}H_7$) derivative yielded the requisite linear geometry.

The reaction of two equivalents of $KC(SiMe_2ONaph)$ with $CoBr_2$ in THF at 60°C affords a green solution. After removal of the solvent in vacuo and redissolution into hexanes, dark red crystals of $Co(C(SiMe_2ONaph)_3)_2$ (**1**) emerged from the green solution over the course of several days at room temperature. Crystallization at –30°C formed green crystals that

were not suitable for X-ray diffraction, but elemental analysis of the thoroughly dried crystals suggested the isolation of the solvated complex, $Co(C(SiMe_2ONaph)_3)_2(THF)$. Compound **1** is insoluble in common organic solvents, and exposure to THF led to formation of a green solution which is likely the aforementioned solvated complex. The zinc congener, $Zn(C(SiMe_2ONaph)_3)_2$ (**2**), was obtained from the reaction of $KC(SiMe_2ONaph)$ and $ZnBr_2$ in Et_2O. After removal of KBr by filtration, colorless crystals of **2** grew from the Et_2O solution over the course of several days. Using the same reaction conditions with a mixture of $ZnBr_2$ and $CoBr_2(THF)$ further enabled preparation of a magnetically dilute sample, $Co_{0.02}Zn_{0.98}(C(SiMe_2ONaph_7)_3)_2$ (**3**).

Single crystal x-ray diffraction analysis revealed compounds **1** and **2** to be isostructural, crystallizing in space group *R*–*3* (no. 148) and featuring a linear C–M–C axis imposed by the S_6 site symmetry (Fig. 1, B and C). The Co–C and Zn–C interatomic distances of 2.066(2) and 1.995(3) Å, respectively, are similar to the Fe–C separation of 2.0505(14) Å in $Fe(C(SiMe_3)_3)_2$ (*12*) and the and Zn–C separation of 1.982(2) Å in $Zn(C(SiMe_3)_3)_2$ (*20*). In addition, the Co···O distance of 3.1051(11) Å and Zn···O distance of 3.1240(16) Å are significantly longer than the sum of cobalt or zinc and oxygen ionic radii (~2.2 Å), suggesting minimal interactions. Instead, the staggered orientation of the ligands facilitates close sp^3-CH···π and sp^2-CH···π contacts of 2.692 and 2.822 Å, respectively (fig. S3), which are in the range of weak CH-π interactions (*21*). This suggests that inter-ligand interactions may help stabilize **1**, consistent with reports of dispersion forces stabilizing other two-coordinate complexes (*22*).

Electronic structure calculations

Ab initio calculations performed on **1** using the crystal structure geometry reveal that the ^4F free ion state is split by the linear ligand field into three doubly-degenerate states $^4\Phi$, $^4\Pi$, and $^4\Delta$, and one non-degenerate state $^4\Sigma^-$ (here we employ $C_{\infty v}$ point group notation). Due to the exceptionally weak ligand field, the seven states of ^4F parentage are split by less than 3000 cm^{-1} (accounting also for interelectron repulsion energy). This splitting is small even relative to that of other two-coordinate complexes; for example, the ^5D and ^4F free ion states of $Fe(C(SiMe_3)_3)_2$ and $[Fe(C(SiMe_3)_3)_2]^-$ are split by 5000 and 6000 cm^{-1}, respectively (*3*, *4*, *7*). Excitations from the $^4\Phi$ ground state of **1** to the $^4\Sigma^-(^4P)$ and $^4\Pi(^4P)$ states were calculated to be spectroscopically accessible at 13,537 and 18,864 cm^{-1}, and indeed are observed in the ultraviolet-visible (UV-vis) diffuse reflectance spectrum at 12,000 and 15,000 cm^{-1} (fig. S4). The splitting of the $^4\Phi$ ground state due to spin-orbit coupling results in four sets of Kramers doublets, best described by $M_J = \pm^9/_2$, $\pm^7/_2$, $\pm^5/_2$, and $\pm^3/_2$, in order of increasing energy. The total splitting of $^4\Phi$ is 1469 cm^{-1}, while the calculated separation between just $M_J = \pm^9/_2$ and $M_J = \pm^7/_2$ is 476 cm^{-1}. Additional calculations performed on a truncated model molecule show that inclusion of the carbon σ-bonding electrons in the complete active space have only a very minor effect (less than 3%) on the energies of both the non-relativistic and relativistic states (tables S10 and S11).

Ligand-field analysis of the calculations revealed the $^4\Phi$ ground state to have the 3d-orbital filling $(d_{x^2-y^2}, d_{xy})^3(d_{xz}, d_{yz})^3(d_{z^2})^1$ (Fig. 2A), which deviates from the expected Aufbau orbital filling of $(d_{x^2-y^2}, d_{xy})^4(d_{xz}, d_{yz})^2(d_{z^2})^1$ ($^4\Sigma^-$) and can be explained by considering the competing effects of ligand field stabilization and interelectron repulsion. In general, interelectronic repulsion is strongest for two electrons occupying the same orbital (necessarily with opposite spin). Two electrons with opposite spin in different orbitals alternatively experience medium-strong electron-electron repulsion, while two electrons with parallel spin (necessarily in different orbitals) repel each other least strongly owing to the presence of the Fermi-hole. Typically, only the electron pairing energy component of interelectron repulsion is important for transition metal complexes, and whether a complex is high- or low-spin is determined by considering whether the ligand field strength is small or large compared to the pairing energy. In the case of **1**, the ligand field strength is so small that not only does the molecule display a high-spin state, but it also maximizes its orbital angular momentum in keeping with the Hund rule for free atoms and ions, thus leading to a non-Aufbau ground state configuration. Clearly, the $(d_{x^2-y^2}, d_{xy})^3(d_{xz}, d_{yz})^3(d_{z^2})^1$ configuration minimizes electron-electron repulsion relative to the alternative $(d_{x^2-y^2}, d_{xy})^4(d_{xz}, d_{yz})^2(d_{z^2})^1$ configuration that features an electronically crowded $(d_{x^2-y^2}, d_{xy})^4$ subshell. This stabilization is also reflected in the total orbital angular momentum of the ground state that is an approximately good quantum number in this system. Non-relativistic ligand field calculations without interelectron repulsion show the expected ground state of $^4\Sigma^-$ (with $L = 0$). Using ligand field parameters from ab initio NEVPT2 calculations and ligand field expressions for the $S = {}^3/_2$ states under linear symmetry with interelectron repulsion, the high orbital angular momentum $^4\Phi$ state (with $L = 3$) is stabilized by 1300 cm^{-1} relative to the $^4\Sigma^-$ state (Fig. 2B and table S9). Spin-orbit coupling further stabilizes the $M_J = {}^9/_2$ component of the $^4\Phi$ ground state by 788 cm^{-1}.

This situation is completely distinct from that of established complexes with stronger ligand fields that can sometimes have electronic ground states with significant contributions from non-Aufbau configurations. For example, the iron(II) metallophthalocyanine complex (FePc) has a ground state with nearly equal contributions from Aufbau and non-Aufbau configurations, wherein the non-Aufbau component arises from an accidental orbital near-degeneracy (*23*). The essential difference between complex **1** and FePc, however, is in ligand field strength, with the two molecules calculated to exhibit total d-orbital splittings of 6000 and

165,000 cm^{-1}, (*23*) respectively. Focusing on the orbitals that give rise to the non-Aufbau states, the $d_{x^2-y^2}$,d_{xy} and d_{xz},d_{yz} orbital pairs are separated by 2900 cm^{-1} in **1**, whereas for FePc the d_{xz},d_{yz} orbital pair and d_{z^2} orbital are separated by 19,000 cm^{-1} (*23*). Our calculations show that interelectron repulsion in **1** easily overwhelms the ligand field stabilization energy associated with the Aufbau configuration, destabilizing the $^4\Sigma^-(^4P)$ state by 12,000 cm^{-1} relative to the $^4\Phi$ state. No similar calculations appear to have been reported for FePc, but it is clear that it would be impossible to observe a pure non-Aufbau ground state as long as the ligand field stabilization energy is of the same magnitude as interelectron repulsion. Once the ligand field requirement for a non-Aufbau ground state is met, it is also possible to observe maximal orbital angular momentum. The maximal orbital angular momentum of $L = 3$ for transition metals requires degenerate $d_{x^2-y^2}$, d_{xy} and d_{xz}, d_{yz} orbital pairs, and thus the molecule should also be linear to avoid Jahn-Teller distortions.

The ligand-field analysis elucidates another challenge in isolating a dialkyl cobalt complex, namely the ligand field stabilization energy suggests that metal-ligand bond formation provides only a minor stabilizing effect of 4.8 kcal/mol (1700 cm^{-1}). This result is perhaps intuitively understood by considering that the formal Co–C bond order is approximately one half, because the d_{xz}, d_{yz} orbitals have slight π-antibonding character and are destabilized primarily by electrostatic interactions. It is not until we consider transmetallic dispersion and electrostatic (CH · · · π) forces that **1** appears to be stable.

Charge density determination

The molecular charge density (CD) of **1** was obtained from multipolar refinement of single crystal x-ray diffraction data measured at 20 K using synchrotron radiation. A small amount of disorder (~6%) is present in the structure due to flipping of the naphthalene groups (also involving the O and Si atoms); however, a detailed description of this disorder was possible and allowed us to extract quantitative information pertinent to the magnetic properties (see methods for a detailed description of the experimental procedure).

The experimental temperature of 20 K is low enough that the CD primarily represents the electronic properties of the relativistic ground state. We used an atom-centered multipole formalism to describe the CD, and thus a complete set of spherical harmonic functions for each atom was used to quantify the deviations from a spherical density distribution. The use of this formalism enables estimation of 3d-orbital populations on the central cobalt atom, under the assumption that the density around the metal originates solely from the atom itself (i.e., that no significant covalent bonding occurs). The parameterized CD also enables an analysis in the framework of quantum theory of atoms in molecules (QTAIM) (*24*) and estimates of atomic charges and the strength of chemical bonding. Defining the local coordination axes such that the Co–C direction is along the *z*-axis, the electron density of the cobalt valence shell is distributed in the following manner: 42.8% is in the $d_{x^2-y^2}$, d_{xy} orbitals, 41.2% is in the d_{xz}, d_{yz} orbitals, and 16.0% is in the d_{z^2} orbital. Furthermore, the same distribution of electrons in the cobalt 3d-orbitals was obtained regardless of the manner in which the naphthalene disorder was treated.

Variable-field far-infrared spectroscopy

We sought to confirm experimentally the magnitude of the separation between the ground and first excited magnetic states in **1** using variable-field far-IR spectroscopy (*25*, *26*). Although such energy separations are more commonly determined by fitting low-temperature magnetization data or high-temperature magnetic relaxation data, these approaches give values that are sensitive to fitting procedures and provide only an indirect measure of the representative ground to excited state energy separation. Additionally, given the calculated energy splitting of 476 cm^{-1} for the lowest M_J states, dc susceptibility measurements would provide limited information on the position of excited states, as the Boltzmann population of the ground state doublet is still 90% at 300 K. Thus, not only is spectroscopy a more direct measurement, but in this case, it is also necessary to gain information on the excited states. Transmission spectra in the 30 to 600 cm^{-1} energy range were collected at a temperature of 4.2 K under applied fields ranging from 0 to 11 T (Fig. 3A). Although absorption bands associated with magnetic dipole transitions are usually significantly weaker than those of electronic dipole transitions, a pronounced field dependence is immediately evident in the data upon dividing the applied field spectra by the zero-field spectrum (Fig. 3B). The only peak visible in this energy range is at 450 cm^{-1} and is attributable to the transition from $M_J = \pm^9/_2$ to $\pm^7/_2$ in good agreement with the calculated separation of 476 cm^{-1}. A steadily increasing blueshift of the IR absorption maximum is observed with increasing applied fields (fig. S5) and is in good agreement with a simulation of the spectral envelope magnetic dipole $M_J = \pm^9/_2$ to $\pm^7/_2$ transitions (fig. S6). In addition to the blueshift there is a concomitant decrease in absorption intensity and peak broadening with increasing field, giving rise to the derivative shape observed in Fig. 3B.

Magnetic properties

Variable-temperature dc magnetic susceptibility data for **1** are shown in Fig. 4A. The gradual decrease in the product of the molar magnetic susceptibility and temperature ($\chi_M T$) with decreasing temperature is indicative of magnetic anisotropy, while the strong field dependence at low temperature arises from an increased Zeeman splitting at higher fields. The room temperature $\chi_M T$ value of 4.89 cm^3 K mol^{-1} is consistent with a well-isolated $M_J = ^9/_2$ ground state (the theoretical $\chi_M T$ value for an isotropic $J = ^9/_2$ ion is 5.47 cm^3 K mol^{-1}), and reduced magnetization plots (Fig. 4B) show a saturation

magnetization of 3.00 μ_B. The simulated $\chi_M T$ and reduced magnetization data from ab initio calculations (solid lines, Fig. 4) are in close agreement with the experimental data, further corroborating the well-isolated $M_J = {}^9/_2$ ground state.

Ac susceptometry was employed to probe magnetic relaxation in the 10^{-4} to 10^{1} s (10^{4} to 10^{-1} Hz) range. By fitting the in-phase (χ') and out-of-phase (χ'') susceptibility (figs. S8 to S11) to a generalized Debye model, we obtained relaxation times for **1**, as shown in the Arrhenius plot in Fig. 5A. The temperature dependence of magnetic relaxation time (τ) in molecules exhibiting slow magnetic relaxation is typically described by the expression

$$\tau^{-1} = \frac{A_1}{1 + A_2 H^2} + BH^4 T + CT^n + \tau_0^{-1} \exp\left(-U/k_B T\right), \quad (1)$$

where the four terms represent quantum tunneling, direct, Raman, and Orbach relaxation processes, respectively (*27*–*29*). However, we were unable to fit the relaxation data for **1** to the total sum of these processes. An alternative model for through-barrier relaxation has recently been proposed, wherein specific phonon modes may facilitate relaxation through direct doublet transitions (*30*, *31*). Building on the results of Lunghi and co-workers, we derived the expression

$$\tau^{-1} = \tau_{\text{tunnel}}^{-1} + \sum_{\alpha} \left(\frac{V_\alpha^2}{\hbar} \frac{\Delta_\alpha \left(2n_\alpha + 1\right)}{\left[\Delta_\alpha^2 + \left(\hbar\omega_\alpha\right)^2\right]} \right) + \tau_0^{-1} \exp\left(-U/k_B T\right), \quad (2)$$

where the first term represents quantum tunneling and the last term represents Orbach relaxation. The second term represents relaxation through the α-th phonon mode, V represents spin-phonon coupling, Δ is the phonon linewidth, n is the phonon occupation number, and ω is the phonon frequency. Both Δ and n are dependent on both temperature and ω. Values for U and ω are taken from the variable-field, far-IR data, while τ_{tunnel}, V, and τ_0 are fit parameters (see eq. S1 to S4 for details). From this equation we were able to obtain reasonable fits (σ_{EST} = 0.17 and 0.21 for **1** and ***3***, respectively) to the relaxation data in Fig. 5A.

To further examine the effect of any tunneling relaxation process, we collected data under a 3000 Oe field. The lack of a temperature-independent region at low temperature under zero and applied field indicates that molecular quantum tunneling is not a dominant relaxation pathway above 4 K; however, the observed increase in relaxation times upon application of a dc field (Fig. 5A) demonstrates that it is a contributing factor. To some extent, the tunneling relaxation rate can be slowed through magnetic dilution (*32*), and indeed measurements of a magnetically dilute sample prepared with a 1:49 ratio of cobalt to zinc (***3***) exhibits lower relaxation rates than **1** under zero field. The lack of a linear temperature dependence at the highest temperatures indicates that two-phonon Orbach relaxation (involving excitation to and relaxation from a real excited state) is not yet dominant at 70 K. Using the value of U = 450 cm^{-1} obtained from far-IR spectroscopy, however, we determined an upper bound for τ_0 of 1.79×10^{-9} s, which is a reasonable value for a single-molecule magnet (*5*).

The low temperature relaxation dynamics of **1** and ***3*** were also probed using dc relaxation and magnetization experiments (Fig. 5B). The tunneling and direct relaxation terms introduced above were used in fits of the variable-field relaxation data and are discussed in detail in the Methods section. The relaxation times extracted at 1.8 K and zero applied field are 16.4 ± 0.7 and 48.2 ± 4.7 s for **1** and ***3***, respectively, and these values slow to 221 and 660 s at 1.8 K under a 1500 Oe applied field. These relaxation times suggest that magnetic hysteresis should be apparent in variable-field magnetization data, and indeed **1** and ***3*** show waist-restricted hysteresis loops between ±0.7 T up to 5 K. A sudden decline in the magnetization as the field approaches zero can be ascribed to rapid relaxation induced by tunneling of the magnetization (Fig. 5, C and D), and this decline results in small values of the remnant magnetization for **1** (0.08 μ_B) and ***3*** (0.28 μ_B) at 1.8 K that diminish to near zero at higher temperatures. Despite the relatively fast relaxation at zero field, **1** has a coercive field, H_c, of 180 Oe at 1.8 K, as measured with a field sweep rate of 32 Oe/s. Under the same conditions, the magnetically dilute sample, ***3***, exhibits H_c = 600 Oe.

Outlook

These results have clear implications toward technologies that require a large magnetic anisotropy. For a magnetic bit to retain its magnetization for information storage, the magnetic anisotropy energy must be significantly greater than the thermal energy. For the cobalt adatom on MgO, the separation between the ground ($M_J = \pm{}^9/_2$) and first excited ($M_J = \pm{}^7/_2$) states was determined to be 468 cm^{-1}, and it was suggested that this value was near a physical limit for magnetic anisotropy for 3d transition metals. This limit can be quantified using the phenomenological spin-orbit coupling Hamiltonian, $H_{SOC} = \lambda \mathbf{L} \cdot \mathbf{S} = ({}^{\zeta}/_{2S}) \Sigma_i \mathbf{l}_i \mathbf{s}_i$, where λ is the effective spin-orbit coupling constant, ζ is the atomic spin-orbit coupling constant, and $\mathbf{L} = \Sigma_i \mathbf{l}_i$ and $\mathbf{S} = \Sigma_i \mathbf{s}_i$ are the operators for the orbital and spin-angular momenta, respectively (the index i sums over individual electrons). In systems with a doubly degenerate ground state, the energies of the M_J states (where $M_J = M_S + M_L$) are given by $E(M_J) = ({}^{\zeta}/_{2S}) M_L \cdot M_S$; the separation between lowest and highest M_J states is equal to $L\zeta$, and the separation between adjacent states is $({}^{L}/_{2S})\zeta$. Thus, the actual limit for the energy separation between ground and first excited state would be found in a system with L = 3 and S = 1. However, in order to maximize relaxation times, it is advantageous to employ half-integer spin systems, as the crystal field cannot couple the two components of the lowest doublet and the tunneling relaxation pathway is therefore suppressed (*33*). The maximal total angular momentum for a

transition metal with half-integer spin is $J = {}^{9}/_{2}$, exhibited by both the cobalt adatom and compound **1**. The magnetic M_J states of **1** span a substantial calculated energy range of 1469 cm^{-1}, and the separation between the ground ($M_J = \pm{}^{9}/_{2}$) and first excited ($M_J = \pm{}^{7}/_{2}$) states alone is 450 cm^{-1}. Within a rigorously linear manifold, it may be possible to further increase the magnetic anisotropy by changing the nature of the Co–L bond and by increasing the spin-orbit coupling constant. However, at present the barrier of U_{eff} = 450 cm^{-1} determined here for **1** is the largest measured to date for any transition metal single-molecule magnet, with the second largest being U_{eff} = 413 cm^{-1} from the aforementioned (sIPr)CoNDmp complex (*15*). Given the similarity between the cobalt adatom and **1**, it is indeed possible that this value is near the physical limit. Our calculations for the Co adatom on MgO indicate that the $^{4}\Phi(^{4}F)$ ground state is also well isolated in this system, suggesting that spin-orbit coupling is also the dominant factor determining the energies of the M_J states here (table S13). Although information storage will certainly require longer zero-field relaxation times than observed here, we note that magnetic relaxation times can be significantly affected by the molecular environment, as has been observed for $Tb(Pc)_2$ molecules in bulk solids (*34*) and on a variety of surfaces (*35–40*). A comparison of the relaxation times of the cobalt adatom on MgO and those of compound **1** indicates such an environmental effect is indeed at play. Both cobalt centers have similar electronic structures, yet the relaxation time for the adatom at 0.6 K is on the order of 10^{-4} s, whereas a much longer relaxation time on the order of 10^{1} s is observed for **1** at 1.8 K.

Beyond the implications for molecular magnetism, an intriguing potential use of the linear $L–Co^{II}–L$ moiety is in the pursuit of lanthanide-free bulk magnets. Generally speaking, orbital angular momentum and spin-orbit coupling tie the magnetic moment to lattice (*41*). In bulk magnetism, orbital angular momentum is responsible for magnetocrystalline anisotropy, the main determinant of magnetic coercivity, which is why the strongest magnets, such as $Nd_2Fe_{14}B$ and $SmCo_5$, feature lanthanide ions with unquenched orbital angular momentum. Our results show how linearly coordinated transition metal ions could provide a similar effect. For example, the extended solid $Li_2(Li_{1-x}Fe_x)N$ features linear iron(I) centers similar to those in $[Fe(C(SiMe_3)_3)_2]^-$, and in high concentration (x = 0.28) this material displays an extremely large coercivity (H_c = 11.6 T at 2 K) (*42*). The magnetic anisotropy of compound **1** is nearly twice as large as in $[Fe(C(SiMe_3)_3)_2]^-$, and incorporation of the $L–Co^{II}–L$ moiety in an extended solid could therefore in principle lead to permanent magnets with an even greater coercivity.

Methods

General considerations

Unless otherwise noted, all manipulations were carried out using standard air-free Schlenk line and glove box techniques under an argon atmosphere. Reagents were purchased from commercial vendors. Anhydrous $CoBr_2$ and $ZnBr_2$ were used as received, while 1-naphthol was sublimed and triethylamine (NEt_3) was dried over KOH and distilled prior to use. $HC(SiMe_2Cl)_3$ (*17*), MeK (*43*) were prepared according to literature procedures. Solvents were dried using a commercial solvent purification system designed by JC Meyer Solvent Systems. Elemental analysis was performed at the Microanalytical Laboratory of the University of California, Berkeley. NMR spectra were collected on a 500 MHz Bruker spectrometer; chemical shifts are reported in ppm referenced to residual protiated solvent.

Synthesis of $HC(SiMe_2OPh)_3$ and $HC(SiMe_2OC_{10}H_7)_3$

A 100 mL Schlenk flask containing a stir bar was charged with a THF solution (50 mL) of $HC(SiMe_2Cl)_3$ (3.73 g, 12.7 mmol) and NEt_3 (1.80 mL, 38.1 mmol). A separate 50 mL Schlenk flask was charged with a THF solution (25 mL) of 1-naphthol (5.58 g, 38.7 mmol). The 1-naphthol solution was added to the reaction flask over the course of several minutes with stirring, and a white precipitate immediately formed upon addition. The reaction was stirred at room temperature for 3 hours, after which air-free techniques were no longer required. Water (20 mL) was added to the reaction flask and the organic layer was collected. The water was extracted with 3×20 mL Et_2O, and the combined organic layers were dried with $MgSO_4$. The ether solvent was removed under reduced pressure, leaving a colorless residue. The residue was washed with MeOH (50 mL) and the resulting white solid, $HC(SiMe_2OC_{10}H_7)_3$ (5.15 g, 66%), was collected by filtration. Anal. calcd for $C_{37}H_{40}O_3Si_3$: C, 72.03; H, 6.54. Found: C, 72.04; H, 6.75. ^{1}H NMR (500 MHz, THF-d8): δ 8.33 (3 H, d), 7.83 (3 H, d), 7.47 (3 H, d), 7.40 (6 H, m), 7.32 (3 H, t), 7.03 (3 H, d), 1.39 (1 H, s), 0.63 (18 H, s) ppm. ^{13}C NMR (500 MHz, THF-d8): δ 151.8, 136.0, 128.9, 128.3, 126.7, 126.4, 125.7, 123.4, 122.0, 114.4, 13.1, 2.9, 2.8 ppm.

The same method was used to synthesize $HC(SiMe_2OPh)_3$, which has been reported previously using a different synthetic method (*44*). The identity of $HC(SiMe_2OPh)_3$ was confirmed by ^{1}H NMR spectroscopy.

Synthesis of $(CH_3OCH_2CH_2OCH_3)_2KC(SiMe_2OPh)_3$

Solid MeK (0.11 g, 1.9 mmol) was slowly added to a stirring solution of **1** (0.91 g, 1.9 mmol) dissolved in Et_2O (10 mL) and dimethoxyethane (3 mL); bubbles evolved during the course of addition. The reaction was then allowed to stir for 3 hours, during which time a white microcrystalline solid precipitated from solution. The solid was collected by filtration and dried under vacuum (0.65 g, 0.95 mmol, 49%). Anal. Calcd for $KC_{33}H_{53}O_7Si_3$: C, 57.85; H, 7.80. Found: C, 57.83; H, 7.60. ^{1}H NMR (500 MHz, THF-d8): δ 7.15 (6 H, t), 6.91 (6 H, d), 6.83 (3 H, t), 3.42 (8 H, s), 3.26 (12 H, s), 0.24 (18 H, s) ppm. ^{13}C NMR (500 MHz, THF-d8): δ 158.3, 129.7, 122.2, 121.0, 72.7,

58.9, 16.8, 15.7, 5.2 ppm.

Synthesis of KC(SiMe$_2$OC$_{10}$H$_7$)$_3$

HC(SiMe$_2$OC$_{10}$H$_7$)$_3$ (0.967 g, 1.57 mmol) was dissolved in THF (15 mL). Freshly prepared MeK (0.0850 g, 1.57 mmol) was added as a solid to the stirring reaction mixture; bubbles evolved from the mixture over the course of an hour. After 3 hours, the reaction mixture was filtered through diatomaceous earth and solvent was removed under reduced pressure, leaving a sticky colorless residue. Hexane was added to precipitate a white solid, KC(SiMe$_2$OC$_{10}$H$_7$)$_3$ (1.20 g, 76%), which was collected by filtration. Anal. calcd for KC$_{37}$H$_{39}$O$_3$Si$_3$: C, 67.84; H, 6.00. Found: C, 67.59; H, 6.31. ^{1}H NMR (500 MHz, THF-d8): δ 8.42 (3 H, d), 7.71 (3 H, d), 7.49 (3 H, d), 7.28 (12 H, m), 0.38 (18 H, s) ppm. ^{13}C NMR (500 MHz, THF-d8): δ 154.8, 135.9, 129.7, 127.7, 126.9, 125.6, 124.4, 124.2, 118.7, 114.5, 16.2, 5.9, 5.8 ppm.

Synthesis of Co(C(SiMe$_2$OPh)$_3$)$_2$

Solid CoCl$_2$ (18.2 mg, 0.140 mmol) was added to a stirring THF solution (10 mL) of (CH$_3$OCH$_2$CH$_2$OCH$_3$)$_2$KC(SiMe$_2$OPh)$_3$ (200. mg, 0.290 mmol) at room temperature and then the mixture was stirred for 2 hours at 60°C. The solvent was removed *in vacuo* and the resulting blue-green solid was dissolved in hexanes. The hexanes solution was stirred at 60°C for 1 hour to form a yellow-green solution. The hexanes solution was filtered through diatomaceous earth and was concentrated *in vacuo*. Red-brown crystals of Co(C(SiMe$_2$OPh)$_3$)$_2$ (0.044 g, 39%) suitable for x-ray diffraction grew in 2 hours at −30°C. Anal. Calcd. for CoC$_{50}$H$_{66}$Si$_6$O$_6$: C, 60.63; H, 6.72. Found: C, 60.98; H, 6.84.

Synthesis of Co(C(SiMe$_2$OC$_{10}$H$_7$)$_3$)$_2$ (1)

Solid CoBr$_2$ (41.6 mg, 0.190 mmol) was added to a stirring THF (8 mL) solution of KC(SiMe$_2$OC$_{10}$H$_7$)$_3$ (249 mg, 0.380 mmol) at room temperature. The reaction mixture was stirred for 4 hours at 60°C, after which time the solution had turned green. The reaction mixture was filtered through diatomaceous earth and solvent was removed under reduced pressure, leaving a green solid. The green solid was dissolved in hexanes (20 mL) and filtered to give an emerald green solution, from which brown-red crystals of **1** (17.8 mg, 7%) suitable for x-ray diffraction grew over the course of 3 days. Compound **1** is insoluble in all common organic solvents except THF, in which it forms a green solution. Anal. calcd for CoC$_{74}$H$_{78}$O$_6$Si$_6$: C, 68.85; H, 6.09. Found: C, 68.36; H, 6.03.

Cooling the green hexanes solution appears to favor precipitation of the THF solvate, Co(C(SiMe$_2$OC$_{10}$H$_7$)$_3$)$_2$(THF). Green crystals not suitable for single crystal x-ray diffraction were grown from the green hexanes solution over 1 day at −30°C, collected by filtration and thoroughly dried *in vacuo*. Anal calcd for CoC$_{78}$H$_{86}$O$_7$Si$_6$: C, 68.74; H, 6.36. Found: C, 68.66; H, 6.52.

Synthesis of Zn(C(SiMe$_2$OC$_{10}$H$_7$)$_3$)$_2$ (2)

At room temperature, a solution of ZnBr$_2$ (35.1 mg, 0.155 mmol) dissolved in THF (2 mL) was added to a solution of KC(SiMe$_2$OC$_{10}$H$_7$)$_3$ (206 mg, 0.314 mmol) dissolved in THF (8 mL), and the mixture was stirred at room temperature for 12 hours. The reaction mixture was subsequently filtered through diatomaceous earth and the THF solvent was removed under reduced pressure, leaving a white solid. The colorless solid was stirred in hexanes (20 mL) and filtered to give a pale-yellow solution, from which colorless crystals of **1** (36.7 mg, 9%) suitable for x-ray diffraction grew over the course of 1 day. Anal. calcd for ZnC$_{74}$H$_{78}$O$_6$Si$_6$: C, 68.51; H, 6.06. Found: C, 68.14; H, 5.92.

Synthesis of Co$_{0.02}$Zn$_{0.98}$(C(SiMe$_2$OC$_{10}$H$_7$)$_3$)$_2$ (3)

Initially, CoBr$_2$(THF) was prepared by dissolving CoBr$_2$ (6.2 mg, 0.028 mmol) in THF (5 mL) and then removing the solvent under reduced pressure. A suspension of CoBr$_2$(THF) (0.028 mmol) and ZnBr$_2$ (57.4 mg, 25.5 mmol) was prepared in Et$_2$O (4 mL), and this suspension was added to a stirring solution of KC(SiMe$_2$OC$_{10}$H$_7$)$_3$ (371 mg, 0.567 mmol) dissolved in Et$_2$O (6 mL). The mixture was stirred for 1 hour at room temperature and then filtered through diatomaceous earth. A light pink powder was collected from the reaction mixture and the resulting light green Et$_2$O filtrate was put in a 20 mL vial. Crystallization tubes were added to the vial to increase the amount of crystallization surfaces and Et$_2$O was added to fill the vial. Light pink crystals of ***3*** (63.9 mg, 9%) suitable for x-ray diffraction grew over the course of 4 days. Successful dilution was confirmed by determination of a unit cell consistent with pure **1** and **2**, and the metal composition was determined from comparison of molar magnetization data for the pure and diluted samples.

Single crystal x-ray diffraction

In an argon filled glovebox, crystals of Co(C(SiMe$_2$OPh)$_3$, **1**, **2**, and ***3*** were coated in Paratone-N oil in individual vials, which were then sealed and remained sealed until immediately prior to mounting. Crystals were mounted on Kaptan loops and cooled under a stream of N$_2$. Data were collected using a Bruker QUAZAR diffractometer equipped with a Bruker MICROSTAR X-Ray source of Mo Kα radiation (λ = 0.71073 Å), and an APEX-II detector. Raw data were integrated and corrected for Lorentz and polarization effects using Bruker Apex3 v. 2016.5. Absorption corrections were applied using SADABS (*45*). The space group was determined by examination of systematic absences, E-statistics, and successive refinement of the structure. The crystal structure was solved with ShelXT (*46*) and further refined with ShelXL (*47*) operated in the Olex2 software (*48*). The crystal did not show any significant decay during data collection. Thermal parameters were refined anisotropically for all non-hydrogen atoms. Hydrogen atoms were placed in ideal positions and refined using a riding model for all structures. A checkcif report for **1** gave rise to a B level alert regarding the ratio of maximum/minimum residual density. The maximum

residual density for **1** lies in the napthyl ring. In the case of the low temperature synchrotron data used for charge density modeling, disorder in the naphthyl ring was successfully modeled. For the data collected at 100 K used for the generation of the cifs for **1** and **2**, we were unable to fully model this disorder, however it is likely that the same disorder is responsible for the relatively large residual density.

UV-visible-NIR diffuse reflectance

UV-visible-NIR diffuse reflectance spectra were collected using a CARY 5000 spectrophotometer interfaced with Varian Win UV software. The samples were prepared in a glovebox and held in a Praying Mantis air-free diffuse reflectance cell. Powdered $BaCO_3$ was used as a non-absorbing matrix. The spectra were collected in $F(R)$ vs wavenumber, where $F(R)$ is the Kubelka-Munk conversion $F(R) = (1 - R)^2/2R$ and R is reflectance.

Magnetometry

All magnetic measurements were carried out using a Quantum Design MPMS-XL SQUID Magnetometer, with the exception of the high frequency ac magnetic susceptibility data. High frequency data (up to 10,000 Hz) was collected at the Quantum Design facility in San Diego, CA, using a 9T PPMS instrument equipped with the ACMSII measurement option to probe the ac moment at frequencies above 1000 Hz. For the measurements using the MPMS instrument, polycrystalline samples of **1** (32.1 mg) and ***3*** (49.7 mg) were loaded into quartz tubes (5 mm i.d., 7 mm o.d.) with a raised quartz platform. Solid eicosane was then added on top of the samples (32.0 and y 61.2, respectively) to prevent crystallite torqueing and provide good thermal contact between the sample and the cryogenic bath. The tubes were fitted with Teflon sealable adapters, evacuated using a glovebox vacuum pump, and sealed under static vacuum using an H_2/O_2 flame. Following flame sealing, the solid eicosane was melted in a water bath held at 40°C. When not in the magnetometer, the sealed samples were stored at −30°C. Dc magnetic susceptibility data was collected for each sample from 2 to 300 K under dc fields ranging from 0 to 7 T. Ac magnetic susceptibility data collected using the MPMS instrument was obtained using a 6 Oe switching field; data from the PPMS instrument was collected using a 10 Oe switching field. All data were corrected for diamagnetic contributions of the eicosane and the individual samples using Pascal's constants (*49*).

The ac susceptibility data was fit using a generalized Debye model, which accounts for relaxation time (τ), attempt time (τ_0), isothermal susceptibility (χ_T), adiabatic susceptibility (χ_S), and the presence of a distribution of relaxation times (α) (*50*). Data for **1** collected under zero applied field and below 7 K exhibited high frequency shoulders in χ'', and fits to the data yielded very large α values, suggesting a second, faster relaxation process might be operating at low temperatures. This second process may be related to the disordered molecules in the crystal. Data from 4 to 10 K were fit with two relaxation processes. Once the minor relaxation process moved out of frequency range of the magnetometer (0.1-1488 Hz), a one process fit was sufficient. The two fitting procedures gave only modestly different τ values for the 4 and 5 K data. The data for ***3*** and the applied field data for **1** were fit sufficiently well with one process. Data collected using the PPMS instrument (50-70 K, 100-10,000 Hz) gave some negative values for χ' at high frequency. Presumably this result is due to the fact that the PPMS sample consisted of less material (6.9 mg **1**, 29.0 mg eicosane) and, especially at high temperatures, exhibited a smaller paramagnetic response relative to the diamagnetic response. The negative values did not affect extraction of relaxation times, however. The method for fitting the relaxation data from 4 to 70 K is given in detail in the ESI.

Dc relaxation measurements were implemented using the hysteresis mode of the MPMS magnetometer, using small magnetizing fields such that the time to set the field was in the 10-30 s range; measurements were made every ~4 s. We found that the relaxation times had a small dependence on the magnetizing field for **1** and a larger dependence for ***3*** (Table S19-20); the times reported in the main text are averages of those times. The relaxation times were determined using a stretched exponential of the form $M_t = M_0 \exp[-(t/\tau)^n]$, where M_0 is the magnetization of the first data point measured, once the field was set, and n is a free variable (*51*).

Dc magnetization experiments were implemented by applying a field to a sample at zero magnetization and measuring the magnetization until it became constant. Relaxation times were determined using the equation $M_t = M_{sat} - (M_{sat} - M_0)\exp[-(t/\tau)^n]$, where M_{sat} is the saturation magnetization, M_0 is the magnetization of the first data point measured once the field was set, and n is a free variable. Magnetization times for **1** and ***3*** for each field are given in tables S20 and S21; the main text reports the average of these values (16.4 and 48.2 s, respectively) and their standard deviations (0.7 and 4.7, respectively).

Variable field, FIR spectroscopy

Far-infrared spectra were recorded on a Bruker IFS 66v/s FTIR spectrometer with a globar source and a composite bolometer detector element located inside an 11 T magnet directly below the sample. Approximately 5 mg of **1** was diluted in eicosane (1:10 ratio) and pressed in the shape of a 5 mm pellet. The sample was prepared and measured under inert atmosphere. The sample was cooled to 4.2 K and irradiated with FIR light. Transmission spectra were recorded both in absence and in the presence of a magnetic field (0-11 T).

Charge density modeling

Crystals of **1** are rather air-sensitive, and thus all crystal manipulation was carried out inside of a glove box under an

Ar atmosphere. A triangularly-shaped single crystal with a maximum dimension of 0.10 mm was selected, and it was mounted using cryo-protecting oil on a pre-centered glass fiber and then rapidly inserted into a cold He stream with a temperature of 20 K, to minimize any risk of air exposure and subsequent crystal decay.

The crystal was mounted on the goniometer of beamline BL02B1 at the SPring8 synchrotron in Japan. The X-ray energy was fixed to 40 keV, corresponding to a wavelength of 0.30988 Å. We have previously experienced significant crystal decay due to radiation damage, and this high energy was chosen in an attempt to avoid this detrimental effect. As shown in fig. S17, the frame scale factor, which accurately captures any crystal decay (as well as other systematic effects, such as beam intensity fluctuations), is scattered relatively close to 1.0, and importantly does not drop off systematically, indicating that there is no significant crystal decay.

The data was collected on a Fuji IP system using 36 ω-scans with a width of 5°, and an overlap of 0.5°, for a total of 180° with a scan speed of 1 min/degree. Given the high symmetry of the compound, this protocol provided a complete data set with sufficient redundancy. The diffraction data ceased to be significant already at $\sin(\theta)/\lambda = 0.9$ Å^{-1}. As we explain below, there is significant dynamic disorder in the crystal structure, which likely results in the lack of high angle data.

The diffraction data were integrated using dedicated Rigaku software RAPID AUTO v2.41, which only integrates the intensity of reflections estimated to be fully present on one frame, i.e., having been rotated fully through the Ewald sphere during one of the 5° rotations. This estimation obviously depends on the mosaicity of the crystal and the desired box size for integration. We experimented with these values in order to optimize the integration results, and those presented herein used mosaicity of 0.7° and a box size of 13×13 pixels. The raw images were scaled to accommodate the different sensitivities of the photomultiplier tubes, an effect which was uncovered in the summer of 2018.

The integration and subsequent scaling in RAPID AUTO provided a total of 43260 reflections, which were then averaged using the point group symmetry –3. This averaged data was reduced to 9008 unique reflections with an average redundancy of 4.8 and a completeness of 99.5%, using the program SORTAV. During refinement, it was noticed that ratio of F(obs) to F(calc) varied systematically, and thus we decided to include ten resolution-dependent scale factors that helped to alleviate this problem, as shown in fig. S19.

These data were used to solve the crystal structure using SHELXT within the Olex2 interface. The structure solution was found to contain a minor, but clearly visible, disordered component, and the disorder is solely in the naphthalene moiety (see fig. S18). The disorder is perhaps best explained as resulting from a mirror symmetry in the plane defined by C(1) (bonded to Co) and partially by Si(1) and O(1). This plane also very nearly includes C(2) (carbon bonded to O(1)). The occupation of the disordered parts is 4.8%, and including this disorder in the model leads to a significant improvement of the refinement.

Despite the significant disorder (one of the consequences of which is that some atoms in the structure are nearly overlapping, we decided to attempt multipole-based charge density modeling. The independent-atom model (IAM) structure from ShelX was exported to the program XD, which is based on the Hansen-Coppens multipole formalism. Herein, we kept the extent of disorder fixed on the values obtained from ShelX, and furthermore used isotropic thermal parameters for the disordered atoms. We did not apply multipole parameters to the disordered atoms, which were kept spherical. Given the nearly whole-molecule disorder, it is imperative to be extremely careful during the refinement procedure. Thus, we used constraints to avoid overfitting, which otherwise is a possibility in such a disordered system. The use of isotropic and spherical disordered atoms helps with this as well.

The final multipole model consists of hexadecapoles on Co and octopoles on all other non-H atoms (except the disordered atoms), while H-atoms were refined using one common monopole and bond-directed dipole. The model was reached after several refinements, in which the level of multipoles was increased by one for each step. Both neutral and ionic scattering factors were tested for Co. In the final model, a neutral scattering factor was used.

In the final refinement, the largest residuals were, as expected, near the Si and the Co atoms. The largest residuals were positive (the largest is around 1.2 eÅ^{-3} and is close to the Co), and significantly larger than the most negative residual density peaks, which were around –0.55 eÅ^{-3}. Such large discrepancy between the positive and negative residuals may indicate that the disorder was not fully accounted for. The Co atom sits on a special position in the space group with a multiplicity of 6, and it is possible that the high residual density at this position is also a result of this high symmetry. The residual near Co does not indicate that the atom sits off-centered. However, it may be related to the disorder and perhaps it does not sit in a harmonic potential. We tried to refine anharmonic thermal parameters, but this refinement had no effect on the residual density.

The residual density distribution, interpreted using the fractal dimensionality plots as first presented by Henn and Meindl (fig. S19) (*52*), shows a somewhat distorted parabola, with a slight tendency to increase more toward the positive residuals. However, this increase is much smaller than expected from the significant residuals near Co and Si, and suggests that despite the disorder, the multipole model may be quantitatively useful.

It is important to note that Co sits on a –3 crystallographic position and therefore only four multipole parameters are symmetry-allowed. The most important parameter in this respect is the quadrupole along the z-axis. However, in the least squares refinement, this parameter correlates strongly with the thermal parameters, including U33, which represents the atomic vibration along the same z-direction. To avoid this correlation, we separated the refinement of multipole parameters from the refinement of atomic positions and vibrations. We first attempted a high angle refinement of the atomic vibrations and positions, but the resulting refinement of multipole parameters led to unphysical values, for instance atomic charges derived from monopole values of more than +2, and κ-parameters deviating by more than 20% from unity. Instead, we chose to use the full data set to independently refine the atomic positions and vibrations of all atoms, subsequently fixing these values and refining the multipole parameters until convergence. This approach represented the final model, from which we extracted the d-orbital population ratios. In the final model, the charge on Co was determined to be +1.3.

REFERENCES AND NOTES

1. I. G. Rau, S. Baumann, S. Rusponi, F. Donati, S. Stepanow, L. Gragnaniello, J. Dreiser, C. Piamonteze, F. Nolting, S. Gangopadhyay, O. R. Albertini, R. M. Macfarlane, C. P. Lutz, B. A. Jones, P. Gambardella, A. J. Heinrich, H. Brune, Reaching the magnetic anisotropy limit of a 3*d* metal atom. *Science* **344**, 988–992 (2014). doi:10.1126/science.1252841 Medline
2. W. M. Reiff, A. M. LaPointe, E. H. Witten, Virtual free ion magnetism and the absence of Jahn-Teller distortion in a linear two-coordinate complex of high-spin iron(II). *J. Am. Chem. Soc.* **126**, 10206–10207 (2004). doi:10.1021/ja030632w Medline
3. J. M. Zadrozny, M. Atanasov, A. M. Bryan, C.-Y. Lin, B. D. Rekken, P. P. Power, F. Neese, J. R. Long, Slow magnetization dynamics in a series of two-coordinate iron(ii) complexes. *Chem. Sci.* **4**, 125–138 (2013). doi:10.1039/C2SC20801F
4. J. M. Zadrozny, D. J. Xiao, M. Atanasov, G. J. Long, F. Grandjean, F. Neese, J. R. Long, Magnetic blocking in a linear iron(I) complex. *Nat. Chem.* **5**, 577–581 (2013). doi:10.1038/nchem.1630 Medline
5. D. Gatteschi, R. Sessoli, J. Villain, *Molecular Nanomagnets* (Oxford Univ. Press, 2006).
6. J. M. Zadrozny, D. J. Xiao, J. R. Long, M. Atanasov, F. Neese, F. Grandjean, G. J. Long, Mössbauer spectroscopy as a probe of magnetization dynamics in the linear iron(I) and iron(II) complexes $[Fe(C(SiMe_3)_3)_2]^{1-/0}$. *Inorg. Chem.* **52**, 13123–13131 (2013). doi:10.1021/ic402013n Medline
7. M. Atanasov, J. M. Zadrozny, J. R. Long, F. Neese, A theoretical analysis of chemical bonding, vibronic coupling, and magnetic anisotropy in linear iron(II) complexes with single-molecule magnet behavior. *Chem. Sci.* **4**, 139–156 (2013). doi:10.1039/C2SC21394J
8. The term "spin-reversal barrier" is somewhat ambiguous in the single-molecule magnet literature. In the systems described here we define it as the separation between ground and first excited M_J (or M_S) states. Thus, "over-barrier" relaxation refers to excitation from $M_J = +J$ to $M_J = +(J - 1)$ states followed by relaxation to the $M_J = -J$ state (an Orbach mechanism). "Through-barrier" relaxation mechanisms are any that allow the system to go from $M_J = +J$ to $M_J = -J$ without excitation to the $M_J = +(J - 1)$ state.
9. M. Atanasov, D. Aravena, E. Suturina, E. Bill, D. Maganas, F. Neese, First principles approach to the electronic structure, magnetic anisotropy and spin relaxation in mononuclear 3d-transition metal single molecule magnets. *Coord. Chem. Rev.* **289–290**, 177–214 (2015). doi:10.1016/j.ccr.2014.10.015
10. P. Zhao, Z. Brown, J. C. Fettinger, F. Grandjean, G. J. Long, P. P. Power, Synthesis and structural characterization of a dimeric cobalt(I) homoleptic alkyl and an iron(II) alkyl halide complex. *Organometallics* **33**, 1917–1920 (2014). doi:10.1021/om500180u
11. P. P. Power, Stable two-coordinate, open-shell (d^1-d^9) transition metal complexes. *Chem. Rev.* **112**, 3482–3507 (2012). doi:10.1021/cr2004647 Medline
12. T. Viefhaus, W. Schwarz, K. Hübler, K. Locke, J. Weidlein, Das unterschiedliche Reaktionsverhalten von basefreiem Tris(trimethylsilyl)methyl-Lithium gegenüber den Trihalogeniden der Erdmetalle und des Eisens. *Z. Anorg. Allg. Chem.* **627**, 715 (2001). doi:10.1002/1521-3749(200104)627:4<715:AID-ZAAC715>3.0.CO;2-0
13. N. H. Buttrus, C. Eaborn, P. B. Hitchcock, J. D. Smith, A. C. Sullivan, Preparation and crystal structure of a two-coordinate manganese compound, bis[(tris(trimethyl)silylmethyl)]manganese. *J. Chem. Soc. Chem. Commun.* **1985**, 1380–1381 (1985). doi:10.1039/c39850001380
14. C.-Y. Lin, J. C. Fettinger, N. F. Chilton, A. Formanuik, F. Grandjean, G. J. Long, P. P. Power, Salts of the two-coordinate homoleptic manganese(I) dialkyl anion $[Mn\{C(SiMe_3)_3\}_2]^-$ with quenched orbital magnetism. *Chem. Commun.* **51**, 13275–13278 (2015). doi:10.1039/C5CC05166F Medline
15. X.-N. Yao, J.-Z. Du, Y.-Q. Zhang, X.-B. Leng, M.-W. Yang, S.-D. Jiang, Z.-X. Wang, Z.-W. Ouyang, L. Deng, B.-W. Wang, S. Gao, Two-coordinate Co(II) imido complexes as outstanding single-molecule magnets. *J. Am. Chem. Soc.* **139**, 373–380 (2017). doi:10.1021/jacs.6b11043 Medline
16. P. E. Kazin, M. A. Zykin, L. A. Trusov, A. A. Eliseev, O. V. Magdysyuk, R. E. Dinnebier, R. K. Kremer, C. Felser, M. Jansen, A Co-based single-molecule magnet confined in a barium phosphate apatite matrix with a high energy barrier for magnetization relaxation. *Chem. Commun.* **53**, 5416–5419 (2017). doi:10.1039/C7CC02453C Medline
17. H. Li, A. J. A. Aquino, D. B. Cordes, F. Hung-Low, W. L. Hase, C. Krempner, A zwitterionic carbanion frustrated by boranes—dihydrogen cleavage with weak Lewis acids via an "inverse" frustrated Lewis pair approach. *J. Am. Chem. Soc.* **135**, 16066–16069 (2013). doi:10.1021/ja409330h Medline
18. S. S. Al-Juaid, C. Eaborn, A. Habtemariam, P. B. Hitchcock, J. D. Smith, K. Tavakkoli, A. D. Webb, The preparation and crystal structures of the compounds $(Ph_2MeSi)_3CMCl$ (M = Zn, Cd, or Hg). *J. Organomet. Chem.* **462**, 45–55 (1993). doi:10.1016/0022-328X(93)83340-2
19. S. S. Al-Juaid, C. Eaborn, S. El-Hamruni, A. Farook, P. B. Hitchcock, M. Hopman, J. D. Smith, W. Clegg, K. Izod, P. O'Shaughnessy, Tris(triorganosilyl)methyl derivatives of potassium and lithium bearing dimethylamino or methoxy substituents at silicon. Crystal structures of $KC(SiMe_3)_2(SiMe_2NMe_2)$, $KC(SiMe_2NMe_2)_3$ and $[LiC(SiMe_3)(SiMe_2OMe)_2]_2$. *J. Chem. Soc. Dalton Trans.* **1999**, 3267–3273 (1999). doi:10.1039/a904043j
20. M. Westerhausen, B. Rademacher, W. Poll, Trimethylsilyl-substituierte Derivate des Dimethylzinks—Synthese, spektroskopische Charakterisierung und Struktur. *J. Organomet. Chem.* **421**, 175–188 (1991). doi:10.1016/0022-328X(91)86402-C
21. M. Nishio, The CH/π hydrogen bond in chemistry. Conformation, supramolecules, optical resolution and interactions involving carbohydrates. *Phys. Chem. Chem. Phys.* **13**, 13873–13900 (2011). doi:10.1039/c1cp20404a Medline
22. C.-Y. Lin, J.-D. Guo, J. C. Fettinger, S. Nagase, F. Grandjean, G. J. Long, N. F. Chilton, P. P. Power, Dispersion force stabilized two-coordinate transition metal–amido complexes of the $-N(SiMe_3)Dipp$ (Dipp = C_6H_3-2,6-Pr^i_2) ligand: Structural, spectroscopic, magnetic, and computational studies. *Inorg. Chem.* **52**, 13584–13593 (2013). doi:10.1021/ic402105m
23. A. J. Wallace, B. E. Williamson, D. L. Crittenden, CASSCF-based explicit ligand field models clarify the ground state electronic structures of transition metal phthalocyanines (MPc; M = Mn, Fe, Co, Ni, Cu, Zn). *Can. J. Chem.* **94**, 1163–1168 (2016). doi:10.1139/cjc-2016-0264
24. R. F. W. Bader, *Atoms in Molecules: A Quantum Theory* (Clarendon Press, 1990).
25. R. Marx, F. Moro, M. Dörfel, L. Ungur, M. Waters, S. D. Jiang, M. Orlita, J. Taylor, W. Frey, L. F. Chibotaru, J. van Slageren, Spectroscopic determination of crystal field splittings in lanthanide double deckers. *Chem. Sci.* **5**, 3287–3293 (2014). doi:10.1039/c4sc00751d
26. Y. Rechkemmer, F. D. Breitgoff, M. van der Meer, M. Atanasov, M. Hakl, M. Orlita, P. Neugebauer, F. Neese, B. Sarkar, J. van Slageren, A four-coordinate cobalt(II) single-ion magnet with coercivity and a very high energy barrier. *Nat. Commun.* **7**, 10467 (2016). doi:10.1038/ncomms10467 Medline
27. D. Gatteschi, R. Sessoli, Quantum tunneling of magnetization and related phenomena in molecular materials. *Angew. Chem. Int. Ed.* **42**, 268–297 (2003).

doi:10.1002/anie.200390099 Medline
28. K. N. Shrivastava, Theory of spin-lattice relaxation. *Phys. Status Solidi B* **117**, 437–458 (1983). doi:10.1002/pssb.2221170202
29. R. Orbach, Spin-lattice relaxation in rare-earth salts. *Proc. R. Soc. London Ser. A* **264**, 458 (1961).
30. A. Lunghi, F. Totti, R. Sessoli, S. Sanvito, The role of anharmonic phonons in under-barrier spin relaxation of single molecule magnets. *Nat. Commun.* **8**, 14620 (2017). doi:10.1038/ncomms14620 Medline
31. A. Lunghi, F. Totti, S. Sanvito, R. Sessoli, Intra-molecular origin of the spin-phonon coupling in slow-relaxing molecular magnets. *Chem. Sci.* **8**, 6051–6059 (2017). doi:10.1039/C7SC02832F Medline
32. S.-D. Jiang, B.-W. Wang, G. Su, Z.-M. Wang, S. Gao, A mononuclear dysprosium complex featuring single-molecule-magnet behavior. *Angew. Chem. Int. Ed.* **49**, 7448–7451 (2010). doi:10.1002/anie.201004027 Medline
33. H. A. Kramers, A general theory of paramagnetic rotation in crystals. *Proc. R. Acad. Sci. Amsterdam* **33**, 959 (1930).
34. M. Gonidec, E. S. Davies, J. McMaster, D. B. Amabilino, J. Veciana, Probing the magnetic properties of three interconvertible redox states of a single-molecule magnet with magnetic circular dichroism spectroscopy. *J. Am. Chem. Soc.* **132**, 1756–1757 (2010). doi:10.1021/ja9095895 Medline
35. L. Margheriti, D. Chiappe, M. Mannini, P.-E. Car, P. Sainctavit, M.-A. Arrio, F. B. de Mongeot, J. C. Cezar, F. M. Piras, A. Magnani, E. Otero, A. Caneschi, R. Sessoli, X-ray detected magnetic hysteresis of thermally evaporated terbium double-decker oriented films. *Adv. Mater.* **22**, 5488–5493 (2010). doi:10.1002/adma.201003275 Medline
36. M. Gonidec, R. Biagi, V. Corradini, F. Moro, V. De Renzi, U. del Pennino, D. Summa, L. Muccioli, C. Zannoni, D. B. Amabilino, J. Veciana, Surface supramolecular organization of a terbium(III) double-decker complex on graphite and its single molecule magnet behavior. *J. Am. Chem. Soc.* **133**, 6603–6612 (2011). doi:10.1021/ja109296c Medline
37. D. Klar, A. Candini, L. Joly, S. Klyatskaya, B. Krumme, P. Ohresser, J.-P. Kappler, M. Ruben, H. Wende, Hysteretic behaviour in a vacuum deposited submonolayer of single ion magnets. *Dalton Trans.* **43**, 10686–10689 (2014). doi:10.1039/C4DT01005A Medline
38. M. Mannini, F. Bertani, C. Tudisco, L. Malavolti, L. Poggini, K. Misztal, D. Menozzi, A. Motta, E. Otero, P. Ohresser, P. Sainctavit, G. G. Condorelli, E. Dalcanale, R. Sessoli, Magnetic behaviour of $TbPc_2$ single-molecule magnets chemically grafted on silicon surface. *Nat. Commun.* **5**, 4582 (2014). doi:10.1038/ncomms5582 Medline
39. J. Dreiser, C. Wäckerlin, M. E. Ali, C. Piamonteze, F. Donati, A. Singha, K. S. Pedersen, S. Rusponi, J. Bendix, P. M. Oppeneer, T. A. Jung, H. Brune, Exchange interaction of strongly anisotropic tripodal erbium single-ion magnets with metallic surfaces. *ACS Nano* **8**, 4662–4671 (2014). doi:10.1021/nn500409u Medline
40. C. Wäckerlin, F. Donati, A. Singha, R. Baltic, S. Rusponi, K. Diller, F. Patthey, M. Pivetta, Y. Lan, S. Klyatskaya, M. Ruben, H. Brune, J. Dreiser, Giant hysteresis of single-molecule magnets adsorbed on a nonmagnetic insulator. *Adv. Mater.* **28**, 5195–5199 (2016). doi:10.1002/adma.201506305 Medline
41. M. Getzlaff, *Fundamentals of Magnetism* (Springer-Verlag, 2008).
42. A. Jesche, R. W. McCallum, S. Thimmaiah, J. L. Jacobs, V. Taufour, A. Kreyssig, R. S. Houk, S. L. Bud'ko, P. C. Canfield, Giant magnetic anisotropy and tunnelling of the magnetization in $Li_2(Li_{1-x}Fe_x)N$. *Nat. Commun.* **5**, 3333 (2014). doi:10.1038/ncomms4333 Medline
43. C. J. Schaverien, A. G. Orpen, Chemistry of (octaethylporphyrinato)lutetium and -yttrium complexes: Synthesis and reactivity of (OEP)MX derivatives and the selective activation of O_2 by $(OEP)Y(.mu.-Me)_2AlMe_2$. *Inorg. Chem.* **30**, 4968–4978 (1991). doi:10.1021/ic00026a023
44. K. D. Safa, S. Tofangdarzadeh, H. H. Ayenadeh, Reactions of tris(dimethylsilyl)methane and polymers containing Si–H groups with various hydroxy compounds under aerobic and mild conditions. *Heteroatom Chem.* **19**, 365–376 (2008). doi:10.1002/hc.20440
45. G. M. Sheldrick, SADABS, version 2.03 (Bruker Analytical X-Ray Systems, 2000).
46. G. M. Sheldrick, SHELXT – integrated space-group and crystal-structure determination. *Acta Crystallogr. A* **71**, 3–8 (2015). doi:10.1107/S2053273314026370 Medline
47. G. M. Sheldrick, Crystal structure refinement with SHELXL. *Acta Crystallogr. C* **71**, 3–8 (2015). doi:10.1107/S0108767307043930 Medline
48. O. V. Dolomanov, L. J. Bourhis, R. J. Gildea, J. A. K. Howard, H. Puschmann, OLEX2: A complete structure solution, refinement and analysis program. *J. Appl. Crystallogr.* **42**, 339–341 (2009). doi:10.1107/S0021889808042726
49. G. A. Bain, J. F. Berry, Diamagnetic corrections and Pascal's constants. *J. Chem. Educ.* **85**, 532 (2008). doi:10.1021/ed085p532
50. K. S. Cole, R. H. Cole, Dispersion and absorption in dielectrics I. Alternating current characteristics. *J. Chem. Phys.* **9**, 341–351 (1941). doi:10.1063/1.1750906
51. C. Sangregorio, T. Ohm, C. Paulsen, R. Sessoli, D. Gatteschi, Quantum tunneling of the magnetization in an iron cluster nanomagnet. *Phys. Rev. Lett.* **78**, 4645–4648 (1997). doi:10.1103/PhysRevLett.78.4645
52. K. Meindl, J. Henn, Foundations of residual-density analysis. *Acta Crystallogr. A* **64**, 404–418 (2008). doi:10.1107/S0108767308006879
53. P.-Å. Malmqvist, B. O. Roos, The CASSCF state interaction method. *Chem. Phys. Lett.* **155**, 189–194 (1989). doi:10.1016/0009-2614(89)85347-3
54. K. Wolinski, P. Pulay, Generalized Möller–Plesset perturbation theory: Second order results for two-configuration, open-shell excited singlet, and doublet wave functions. *J. Chem. Phys.* **90**, 3647–3659 (1989). doi:10.1063/1.456696
55. K. Andersson, P. A. Malmqvist, B. O. Roos, A. J. Sadlej, K. Wolinski, Second-order perturbation theory with a CASSCF reference function. *J. Phys. Chem.* **94**, 5483–5488 (1990). doi:10.1021/j100377a012
56. K. Andersson, P. Å. Malmqvist, B. O. Roos, Second-order perturbation theory with a complete active space self-consistent field reference function. *J. Chem. Phys.* **96**, 1218–1226 (1992). doi:10.1063/1.462209
57. B. O. Roos, P.-A. Malmqvist, Relativistic quantum chemistry: The multiconfigurational approach. *Phys. Chem. Chem. Phys.* **6**, 2919 (2004). doi:10.1039/b401472n
58. B. Roos, M. Fülscher, P.-Å. Malmqvist, M. Merchán, L. Serrano-Andrés, "Theoretical studies of the electronic spectra of organic molecules," in *Quantum Mechanical Electronic Structure Calculations with Chemical Accuracy*, S. Langhoff, Ed. (Springer Netherlands, 1995), pp. 357–438.
59. C. Angeli, R. Cimiraglia, S. Evangelisti, T. Leininger, J.-P. Malrieu, Introduction of n-electron valence states for multireference perturbation theory. *J. Chem. Phys.* **114**, 10252–10264 (2001). doi:10.1063/1.1361246
60. C. Angeli, R. Cimiraglia, J.-P. Malrieu, N-electron valence state perturbation theory: A fast implementation of the strongly contracted variant. *Chem. Phys. Lett.* **350**, 297–305 (2001). doi:10.1016/S0009-2614(01)01303-3
61. C. Angeli, R. Cimiraglia, J.-P. Malrieu, N-electron valence state perturbation theory: A spinless formulation and an efficient implementation of the strongly contracted and of the partially contracted variants. *J. Chem. Phys.* **117**, 9138–9153 (2002). doi:10.1063/1.1515317
62. C. Angeli, B. Bories, A. Cavallini, R. Cimiraglia, Third-order multireference perturbation theory: The *n*-electron valence state perturbation-theory approach. *J. Chem. Phys.* **124**, 054108 (2006). doi:10.1063/1.2148946 Medline
63. F. Neese, The ORCA program system. *Wiley Interdiscip. Rev. Comput. Mol. Sci.* **2**, 73–78 (2012). doi:10.1002/wcms.81
64. Max Planck Institute for Chemical Energy Conversion, ORCA, an ab initio, DFT and semiempirical SCF-MO package, version 4.0; https://orcaforum.cec.mpg.de/.
65. F. Neese, Efficient and accurate approximations to the molecular spin-orbit coupling operator and their use in molecular g-tensor calculations. *J. Chem. Phys.* **122**, 034107 (2005). doi:10.1063/1.1829047 Medline
66. D. Ganyushin, F. Neese, First-principles calculations of zero-field splitting parameters. *J. Chem. Phys.* **125**, 24103 (2006). doi:10.1063/1.2213976 Medline
67. M. Atanasov, D. Ganyushin, K. Sivalingam, F. Neese, A modern first-principles view on ligand field theory through the eyes of correlated multireference wavefunctions. *Struct. Bond.* **143**, 149–220 (2012). doi:10.1007/430_2011_57
68. S. K. Singh, J. Eng, M. Atanasov, F. Neese, Covalency and chemical bonding in transition metal complexes: An ab initio based ligand field perspective. *Coord. Chem. Rev.* **344**, 2–25 (2017). doi:10.1016/j.ccr.2017.03.018
69. J. R. Burdett, *Molecular Shapes: Theoretical Models of Inorganic Stereochemistry* (Wiley, 1980).

ACKNOWLEDGMENTS

We thank K. R. Meihaus for editorial assistance. **Funding:** This work was funded by

NSF grant CHE-1464841 (P.C.B., J.R.L.), Max-Planck Gesellschaft (M.A., F.N.), DNRF93 and Danscatt (E.D.-M., J.O.), and DFG SL104/5-1 (M.P., J.V.S.). **Author contributions:** Synthesis, magnetic characterization, and analysis were performed by P.C.B. and J.R.L. Ab initio calculations and analysis were performed by M.A. and F.N. Applied-field FIR spectra were collected and analyzed by M.P., I.C., M.O., and J.V.S. Charge density data collection and modeling were performed by E.D.-M. and J.O. **Competing interests:** The authors have no competing interests to claim. **Data and materials availability:** Crystallographic data for **1**, **2**, and $Co(C(SiMe_2OPh)_3)_2$ are freely available from the Cambridge Crystallographic Data Centre under CCDC numbers 1872361, 1872361, and 1872363, respectively. The supplementary materials include details on the fitting of magnetic relaxation data, as well as computational methods.

SUPPLEMENTARY MATERIALS

www.sciencemag.org/cgi/content/full/science.aat7319/DC1
Materials and Methods
Figs. S1 to S19
Tables S1 to S22
References (*53*–*69*)

28 March 2018; resubmitted 2 August 2018
Accepted 1 November 2018
Published online 15 November 2018
10.1126/science.aat7319

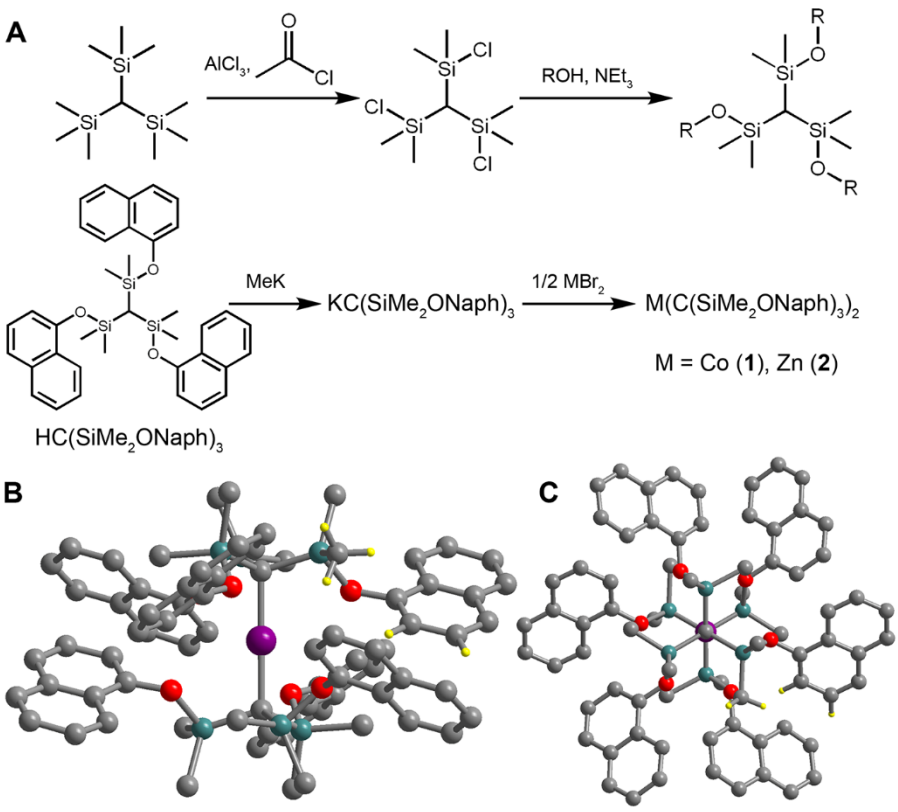

Fig. 1. Synthesis and structure of linear Co and Zn dialkyl complexes. (**A**) General synthetic scheme for ligands of the type $HC(SiMe_2OR)_3$ and synthesis of compounds **1** and **2**. (**B**) Molecular structure of $Co(C(SiMe_2ONaph)_3)_2$ (**1**). Purple, gray, turquoise, red, and yellow spheres represent Co, C, Si, O, and H atoms, respectively. Most hydrogen atoms have been omitted for clarity. Hydrogen atoms are shown on three carbons to illustrate the location of the CH-π interactions. (**C**) Molecular structure of $Co(C(SiMe_2ONaph)_3)_2$ viewed along the molecular *z*-axis.

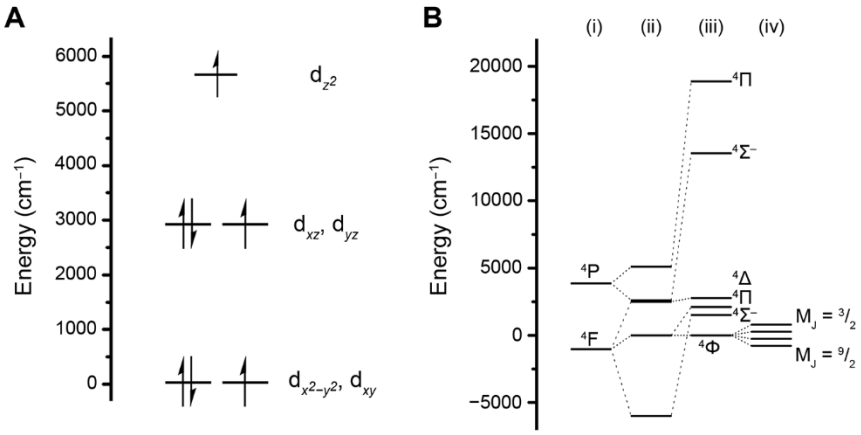

Fig. 2. Electronic structure analysis. (**A**) Energy diagram depicting the energy and electron occupations of the 3d-orbitals based on ligand field analysis of *ab initio* calculations. (**B**) Electronic structure of (i) a free Co(II) ion, (ii) Co(C(SiMe$_2$ONaph)$_3$)$_2$ (**1**) considering only ligand field interactions, (iii) Co(C(SiMe$_2$ONaph)$_3$)$_2$ considering both ligand field interactions and interelectron repulsion, and (iv) the splitting of the ground $^4\Phi$ state of Co(C(SiMe$_2$ONaph)$_3$)$_2$ due to spin orbit coupling according to *ab initio* calculations. Term symbols are for $C_{\infty v}$ symmetry. The splitting between the ground $M_J = {}^9/_2$ and maximal excited $M_J = {}^3/_2$ states is 1469 cm^{-1}.

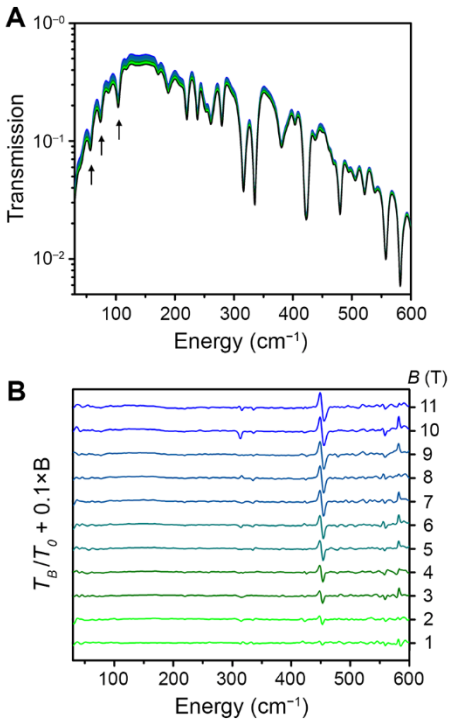

Fig. 3. Variable-field, far-IR spectroscopy. (**A**) Absolute transmission spectra for **1** collected at 4.2 K under applied fields ranging from 0 to 11 T. Phonon energies used in Eq. 2 to describe magnetic relaxation are marked with arrows. (**B**) Plots of applied field spectra divided by the zero-field spectrum. The peak at 450 cm^{-1} corresponds to the transition from $M_J = {}^9/_2$ to $M_J = {}^7/_2$.

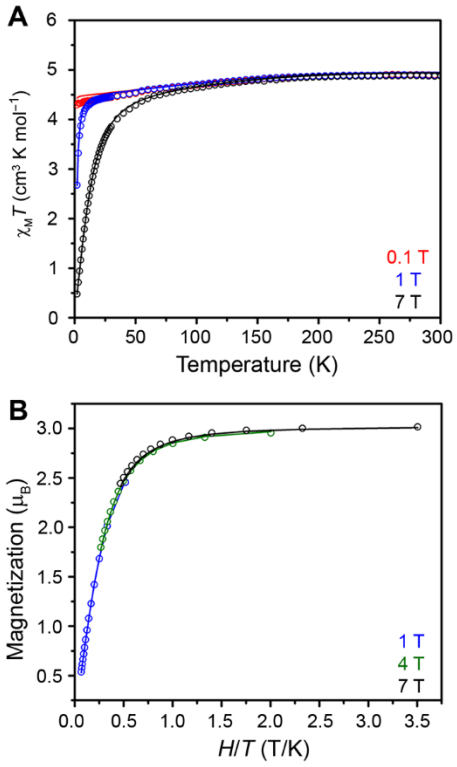

Fig. 4. Magnetic susceptibility and reduced magnetization analysis. (**A**) Variable-temperature molar magnetic susceptibility times temperature ($\chi_M T$) for **1** collected under dc fields of 0.1, 1, and 7 T; solid lines are simulated data from ab initio calculations. (**B**) Reduced magnetization data for **1** collected at temperatures from 2 to 15 K under dc fields of 1, 4, and 7 T; solid lines are simulated data from ab initio calculations.

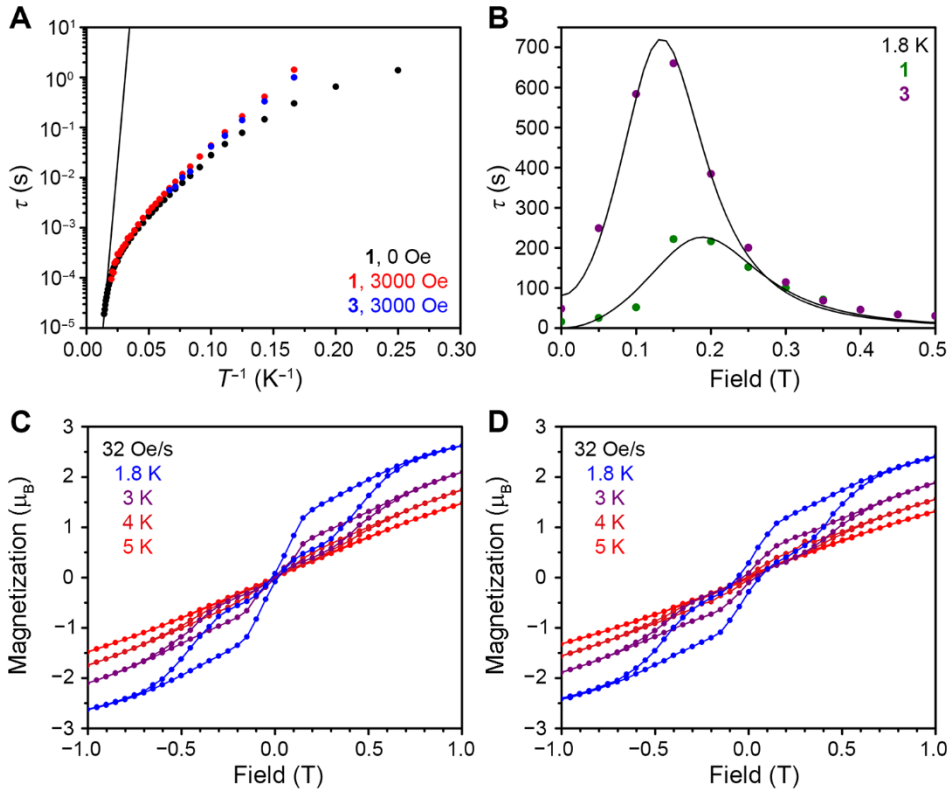

Fig. 5. Magnetic relaxation dynamics. (**A**) Arrhenius plot showing the natural log of relaxation time, τ, versus inverse temperature for **1** in the absence of an applied dc field (black circles), **1** under a 3000 Oe dc field (red circles), and **3** in the absence of an applied dc field (blue circles). Relaxation times are determined from fits of ac susceptibility measurements over the temperature range of 4 to 70 K. The purple and green lines represent fits of the relaxation data for **1** under 0 and 3000 Oe, respectively. (**B**) Dc relaxation and magnetization times for **1** (green circles) and **3** (purple circles). The solid lines are from fits describing relaxation via tunneling and direct relaxation processes as described in the text and Methods. (**C**) Variable-field magnetization data for **1** collected at temperatures ranging from 1.8 to 5 K at a field sweep rate of 32 Oe/s. (**D**) Variable-field magnetization data for **3** collected at temperatures ranging from 1.8 to 5 K at a field sweep rate of 32 Oe/s.

A linear cobalt(II) complex with maximal orbital angular momentum from a non-Aufbau ground state

Philip C. Bunting, Mihail Atanasov, Emil Damgaard-Møller, Mauro Perfetti, Iris Crassee, Milan Orlita, Jacob Overgaard, Joris van Slageren, Frank Neese and Jeffrey R. Long

published online November 15, 2018